Microstructural evolution at interfaces of thermal barrier coatings during isothermal oxidation

Y.Z. Liu [a,b], S.J. Zheng [b,*], Y.L. Zhu [b], H. Wei [c], X.L. Ma [b,*]

[a] *School of Chemistry and Materials Science, University of Science and Technology of China, Hefei 230026, China*
[b] *Shenyang National Laboratory for Materials Science, Institute of Metal Research, Chinese Academy of Sciences, Shenyang 110016, China*
[c] *Superalloys Division, Institute of Metal Research, Chinese Academy of Sciences, Shenyang 110016, China*

ABSTRACT

Using transmission electron microscopy, we investigate microstructural evolution at interfaces of a plasma sprayed thermal barrier coating system with an yttria–stabilized zirconia top coat and a NiCrAlY bond coat after isothermal oxidation at 1100 °C for up to 50 h. Interestingly, thermally grown oxide (TGO) layers split into two sub-layers. In principle, one of the two sub-layers comprises a mixture of α-Al_2O_3, Cr_2O_3 and $Ni(Al, Cr)_2O_4$, while the other one consists of dense α-Al_2O_3 and Cr_2O_3. Main microstructural evolution of the TGO layers follows a similar sequence that: original phases $\rightarrow$ α-Al_2O_3 + Cr_2O_3 $\rightarrow$ α-Al_2O_3 + Cr_2O_3 + $Ni(Al, Cr)_2O_4$. Particularly, after 50 h oxidation, γ-Ni and NiO form in the upper TGO sub-layer at the top coat–bond coat interface, and γ-Ni and α-Cr form in the upper TGO sub-layer at the bond coat-substrate interface. Moreover, γ-Al and β-Ti precipitate at the TGO-substrate interface after 50 h oxidation.

1. Introduction

Thermal barrier coatings (TBCs) fabricated via electron beam physical vapor deposition (EB-PVD) [1,2] or air/vacuum plasma spray (A/VPS) [3] are widely used as surface protection systems in jet engines and gas turbines, because they can enhance the overall engine efficiency by increasing the operating temperature up to 200 °C [4,5]. Usually, the TBCs consist of a ceramic top coat, primarily acting as a thermal insulator to reduce the heat transfer to metallic substrates [6], and a metallic bond coat, which protects the substrates from high temperature oxidation and/or corrosion and joins the top coat and the substrates firmly. For over 30 years yttria partially stabilized zirconia (YSZ) has been the prime choice for ceramic top coat owing to the fact that its thermal conductivity is over one order of magnitude lower than that of Ni-based superalloys. In regard to bond coats, both MCrAlY-type (M = Fe, Co and/or Ni) overlays [7] and Pt modified aluminide coatings [8] are prevailing. Additionally, when the TBCs are in service, thermally grown oxide (TGO) layers often form as a result of oxidation of bond coats.

Although different mechanisms that control TBCs failure have been reported, generally accepted key factors are mismatch of thermal-expansion coefficient between ceramic top coats and bond coats, oxidation, and continuous change in compositions, microstructures, interfacial morphologies derived by the element interdiffusion between coats and superalloy substrates [1]. The above key factors are shown simultaneously at the interfaces due to dramatic composition change, the highest thermal-expansion mismatch and severe stress concentration at the interfaces, thus making the interfaces the weakest sites of TBCs. For example, the TGO formed at the top coat–bond coat interface has been identified as the driving force for coating degradation when a TBC is thermally exposed at high temperatures [9]. Using micro-mechanical test the TBC failures have been investigated intensively (e.g. [10,11]), however, interfacial behaviors, such as element segregation and phase evolution which are important sources of mechanical stress, have not been paid enough attention.

Despite the fact that a few studies have investigated the interfacial behaviors of TBCs systems, they only focused on either top coat–bond coat interfaces [12–14] or bond coat-substrate interfaces [11,15]. As a complete TBC system, interaction among top coats, bond coats and substrates always occur. For instance, element interdiffusion usually exhibits a continuous gradient across top coat–bond coat-substrate interfaces, and the oxidation process relies on penetrating of O from the environment through top coat and bond coat to the substrate, thus performance of the top coat–bond coat interface will influence that of the bond coat–substrate interface. Hence it is necessary to study both top coat–bond coat and bond coat–substrate interfaces simultaneously

* Corresponding author. Fax: +86 2423891320.
E-mail addresses: sjzheng@imr.ac.cn (S.J. Zheng), xlma@imr.ac.cn (X.L. Ma).
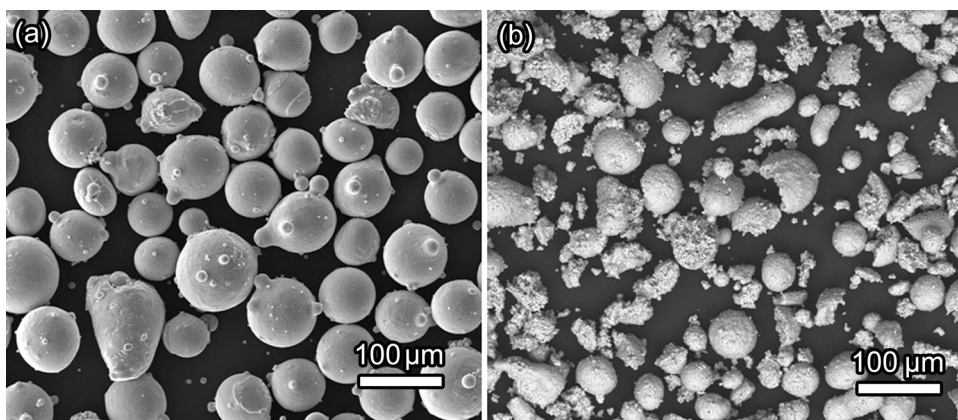
Fig. 1. SEM images showing the morphologies of (a) Metco Amdry 962 (Ni-22Cr-10Al-1Y,wt%) and (b) AI-1075 (ZrO$_2$–8Y$_2$O$_3$,wt%) powders, used for fabrication of the bond coat and the top coat, respectively.

in a complete TBC system. To our best knowledge, the only work covering both top coat–bond coat and bond coat–substrate interfaces of a complete TBC system was conducted by Wu and Reed [16], which implies that TBC compatibility depends upon substrate composition. However, they [16] did not provide any information about microstructural evolution.

To study the entire process of the failures of TBCs, long time-intervals of thermal oxidations have often been used [16,17]. For example, Wu and Reed [16] studied the compatibility of super-alloy with a TBC system after 100 h, 250 h and 500 h oxidation. Schilbe [17] investigated element diffusion of substrate alloy in a TBC system after cyclic oxidation at 1408 K for 400, 600 and 1050 cycles. However, structural changes at the initial stage which is crucial to understand the failure mechanisms could be missed since structural evolution can happen in just a few hours. Therefore, it is necessary to investigate the interfacial behaviors with a short time-interval, especially in the early oxidation stage.

As for analyzing microstructural evolution, transmission electron microscopy (TEM) can not only provide basic morphology and phase information, but also supply elemental mapping over a large area with a high spatial resolution when working in the model of scanning transmission electron microscopy combining energy-dispersive X-ray spectroscopy (STEM-EDS). Although TEM has such a big advantage on studying microstructures, previous researches [18–20] only implemented TEM on top coat–bond coat interfaces at one stage of oxidation process as a result of difficulty in preparation of cross-sectional TEM specimens [21]. Consequently, it is meaningful to technically elucidate structural evolution at all interfaces of a complete TBC system and at as many early stages as possible.

The aim of this work is to analyze in depth the interfacial microstructure evolution of a plasma sprayed TBC system by a combination of scanning electron microscopy (SEM), X-ray diffraction (XRD), TEM and STEM-EDS. The initial interfaces among top coat, bond coat, and substrate, as well as TGO layers formed at the initial interfaces after a series of isothermal oxidation at 1100 °C, all are named as interfaces here and investigated systematically. The results of this study will be helpful to understand the failure mechanism of TBC systems.

2. Experiments

2.1. Sample fabrication

A Ni-based single crystal superalloy with a composition of 8Co–8Cr–8W–6Ta–5Al–1Ti–0.001P–0.0005S (wt%) was used as the substrate, which has a diameter of 40 mm and a thickness of 3 mm. Metco Amdry962 (Ni–22Cr–10Al–1Y, wt%; Sulzer Metco Inc., New

Table 1
Spray parameters for bond coat (NiCrAlY) and top coat (YSZ).

Spray parameters	NiCrAlY (VPS)	YSZ (APS)
Current (A)	500	650
Voltage (V)	125	160
Pressure of primary gas Ar (MPa)	0.52	0.48
Pressure of second gas H$_2$ (MPa)	0.45	0.41
Flow rate of primary gas Ar (m^3/h)	2.83	2.55
Flow rate of second gas H$_2$ (m^3/h)	0.42	0.57
Powder feeding rate (g/min)	30	25
Spray distance (mm)	150	100
Pressure of the spraying chamber (Pa)	10^3	

York, USA) and AI-1075 (ZrO$_2$–8Y$_2$O$_3$, wt%; Praxair Surface Technologies Inc., Indiana, USA) powders were used for fabrication of the bond coat and the top coat, respectively. The nominal diameters of the Metco Amdry962 and AI-1075 powders are 25–75 μm as shown in the typical SEM images of Fig. 1.

Before coating fabrication, surfaces of the substrates were grit-blasted with an 8070P-B sandblasting machine (sand specifications: 0.3 mm white corundum (α-Al$_2$O$_3$); blasting strength: 0.7 MPa) so as to facilitate bonding of the coatings, then cleaned via ethanol and acetone mixture in a KQ-100B type ultrasonic cleaning machine, finally dried by a DHG-9031 type electric thermostatic drying oven.

Afterwards, the grit-blasted substrates were interposed into a special chucking appliance and preheated to the spraying temperature. The TBC system was deposited by a Metco 9 M PS machine equipped with a vacuum plasma spray (VPS) system. First, using a VPS process, a NiCrAlY bond coat with a thickness of 50–70 μm was fabricated via the Metco Amdry962 powder. Then, by air plasma spraying (APS), a YSZ top coat with a thickness of 100–150 μm was sprayed via the Metco 204B-NS powder. The spray parameters are listed in Table 1.

2.2. Isothermal oxidation

Using an improved SNOL 4/1100LSC01 furnace equipped with temperature and time control instrument, isothermal oxidation experiments were performed at 1100 °C in static air. Specimens were respectively mounted in crucibles and put into the furnace at room temperature (22 ± 0.5 °C), then heated to 1100 °C in 40 min, at last, removed from the furnace and cooled down to room temperature with a fan after each holding time.

Nineteen holding times, 0.5 h, 1–10 h ($\Delta t = 1$ h), 15–50 h ($\Delta t = 5$ h) were set for the oxidation. For each holding time 5 samples were oxidized simultaneously. Although all samples were
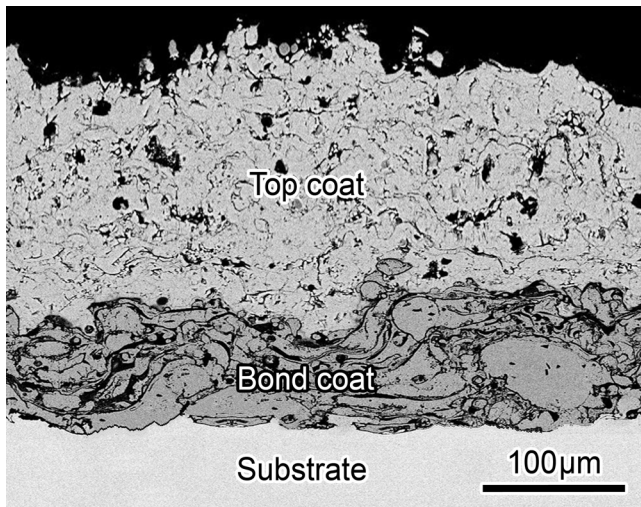
Fig. 2. An SEM image showing cross-sectional microstructure of the as-sprayed TBC system.

studied, only TEM results acquired from samples with holding times of 5 h, 10 h, 25 h and 50 h will be presented since they are corresponding to critical structural changes.

2.3. Microstructural characterization

Cross-sectional metallographic samples were prepared by a conventional method. The samples were cut with a low speed diamond saw and then ground using 5000 grit SiC paper, followed by polishing in diamond slurry up to a 0.5 μm finish. Polished surfaces were cleaned by deionized water, then by ultrasonic cleaning in acetone and ethanol. These obtained samples were examined using a SEM that operating at high-vacuum condition (FEI Inspect F50). XRD analyses were performed in a Philips PW3040/00 X'Pert MPD/MRD diffractometer using Cu Kα.

Cross-secional TEM samples were prepared by a conventional cross-sectioning method consisting of mechanical thinning and ion milling on a Gatan precision ion polishing system (PIPS). An FEI Tecnai G2 F30 equipped with a high-angle annular dark-field detector (HAADF) and an EDS system was used for conventional TEM characterization and STEM-EDS analysis.

3. Results

3.1. Interfaces of as-sprayed TBC systems

Fig. 2 shows a typical morphology of the as-sprayed TBC system comprising a 60 μm thick NiCrAlY bond coat and a 110 μm thick YSZ top coat. Thin and large splats exist in the TBC system due to the deposition of individual molten droplets. Fig. 3 displays XRD patterns of the as-sprayed TBC system obtained at different depths below the surface. The as-sprayed top coat mainly consists of tetragonal YSZ (t-YSZ, $P4_2/nmc$ space group, $a = b = 0.361$ nm, $c = 0.518$ nm), tetragonal prime YSZ (t′-YSZ, $P4_2/nmc$ space group, $a = b = 0.508$ nm, $c = 0.518$ nm) and cubic YSZ (c-YSZ, $Fm\bar{3}m$ space group, $a = 0.513$ nm). γ-Ni ($Fm\bar{3}m$, $a = 0.352$ nm), β-NiAl ($Pm\bar{3}m$, B2 structure, $a = 0.287$ nm) and Al_2Y ($Fd\bar{3}m$, $a = 0.786$ nm) constitute the main phases of the bond coat. The single crystal Ni-based substrate is composed of γ-Ni and γ′-Ni_3Al ($Pm\bar{3}m$, ordered $L1_2$ structure, $a = 0.357$ nm). All the phase compositions agree with previous studies [22–27] and what we designed.

Fig. 4 illustrates the element maps at the top coat–bond coat interface and the corresponding selected area electron diffraction (SAED) patterns of primary phases in the as-sprayed TBC system.

Fig. 4a is a HAADF-STEM image of the interface. Main elements of the top coat are O (Fig. 4b), Y (Fig. 4f) and Zr (Fig. 4g). The main constituents of the as-sprayed YSZ top coat are t-YSZ (Fig. 4h, region marked with "A" in Fig. 4a), t′-YSZ (Fig. 4i, region marked with "B" in Fig. 4a) and c-YSZ (Fig. 4j, region marked with "C" in Fig. 4a), while Y_2O_3 (Fig. 4k, "D" in Fig. 4a) also can be seen occasionally around the top coat–bond coat interface. The bond coat contains Al (Fig. 4c), Cr (Fig. 4d), Ni (Fig. 4e) and Y (Fig. 4f) which comprise the original powder. In the NiCrAlY bond coat, regions marked with "E", "F" and "G" can be identified as β-NiAl (Fig. 4l), Al_2Y (Fig. 4m) and γ-Ni (Fig. 4n) respectively. As indicated by Figs. 4a, c–e, most Cr appears as a solid solution element in β-NiAl and γ-Ni. All those above are consistent with the XRD results in Fig. 3.

Compared with the top coat–bond coat interface, Fig. 5 displays the elemental distribution and phases at a representative bond coat–substrate interface. The bond coat–substrate interface can be determined by the distribution of Co (Fig. 5d), Ta (Fig. 5g) and W (Fig. 5h) because they only appear in the substrate. The same as illustrated in Fig. 4, the bond coat mainly consists of β-NiAl (Fig. 5i), Al_2Y (Fig. 5j) and γ-Ni (Fig. 5k). Additionally, the substrate is predominantly composed of γ and γ′ (Fig. 5l). Again, this is in good agreement with the XRD results in Fig. 3.

3.2. Microstructural evolution at the top coat–bond coat interface during oxidation

Fig. 6 exhibits the element maps of the top coat–bond coat interface and SAEDs of dominant phases in the TGO layer after oxidation at 1100 °C for 5 h. It is found that O (Fig. 6b) and Al (Fig. 6c) highly concentrate in the TGO layer, while Cr (Fig. 6d), Ni (Fig. 6e), Y (Fig. 6f) and Zr (Fig. 6g) only segregate locally at the interface between the TGO layer and the top coat. Identified by SAED analysis, the main phase of the TGO layer is α-Al_2O_3 (Fig. 6h). Notably, β-NiAl and Al_2Y in the as-sprayed bond coat have disappeared in the vicinity of the TGO-bond coat interface because of internal oxidation.

As shown in Fig. 7a, compared with the 5 h oxidation, the TGO layer presents two sub-layers as indicated by a dashed line after oxidation at 1100 °C for 10 h. Both sub-layers are composed of O (Fig. 7b), Al (Fig. 7c), and Cr (Fig. 7d), which are identified as α-Al_2O_3 and Cr_2O_3 (Fig. 7h) by SAED analysis. The difference between the two sub-layers is that the grain size in the upper sub-layer is smaller than that in the lower sub-layer. Moreover, Ni (Fig. 7e) does not appear in the TGO layer.

Fig. 8 depicts STEM–EDS element maps of the top coat–bond coat interface after oxidation at 1100 °C for 25 h. The upper TGO sub-layer comprises O (Fig. 8b), Al (Fig. 8c), Cr (Fig. 8d), and Ni (Fig. 8e), which form spinel $Ni(Al, Cr)_2O_4$ (Fig. 8h, marked with "A" in Fig. 8a), as well as α-Al_2O_3 and Cr_2O_3. More EDS analysis which is not showed here demonstrates that in the spinel $Ni(Al, Cr)_2O_4$ phase, content of Al is usually much higher than that of Cr. While, the lower TGO sub-layer still mainly comprises O, Cr, and Al, which preserve the previous α-Al_2O_3 and Cr_2O_3. Y (Fig. 8f) and Zr (Fig. 8g) diffuse sporadically into the upper TGO sub-layer.

With further extension of oxidation time to 50 h, as shown in Fig. 9, the entire TGO layer still presents the sub-layer structure. Except α-Al_2O_3, Cr_2O_3, and $Ni(Al, Cr)_2O_4$ already existed in the 25 h oxidized sample, γ-Ni (Fig. 9a) and NiO (Fig. 9h) emerge in the upper TGO sub-layer. It is worth noting that the γ-Ni does not contain solid solution element Cr, suggesting Cr depletion by oxidation.

3.3. Microstructural evolution at the bond coat-substrate interface during oxidation

Based on a lot of results from the samples with holding times from 0.5 h to 10 h, TGO does not appear at the bond coat–substrate interfaces before 10 h oxidation. After 10 h oxidation, TGO forms
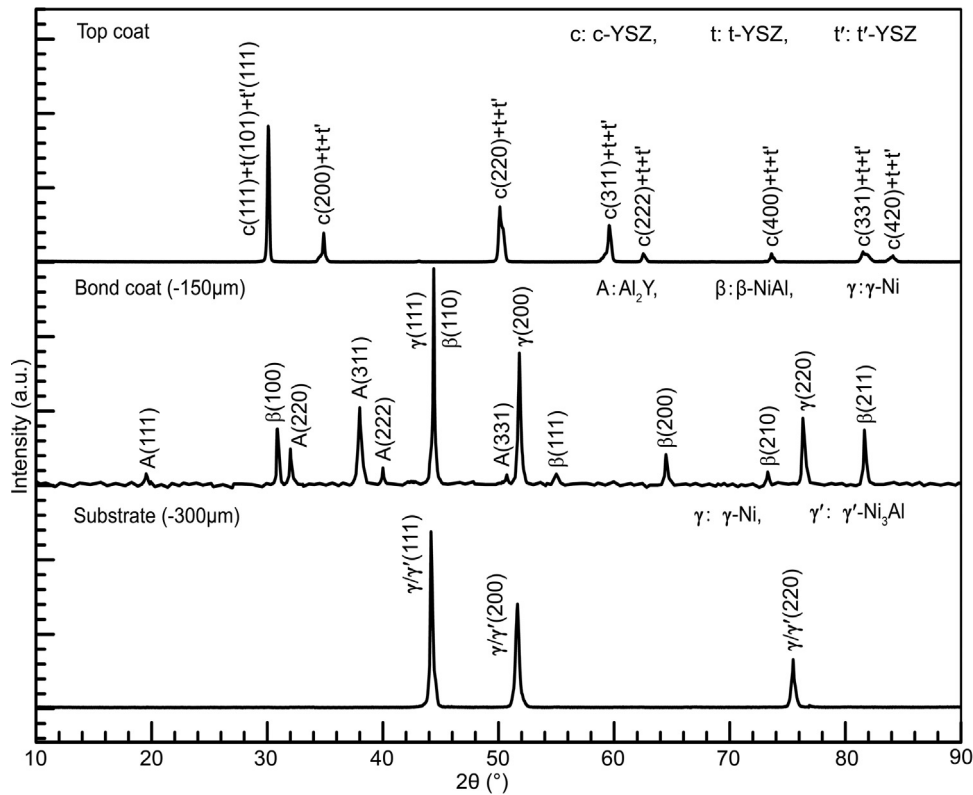
Fig. 3. XRD patterns of the as-sprayed TBC system obtained at different depths below the surface: (a) top coat, (b) bond coat (about 150 μm beneath the surface of the top coat) and (d) substrate (about 300 μm beneath the surface of the top coat).
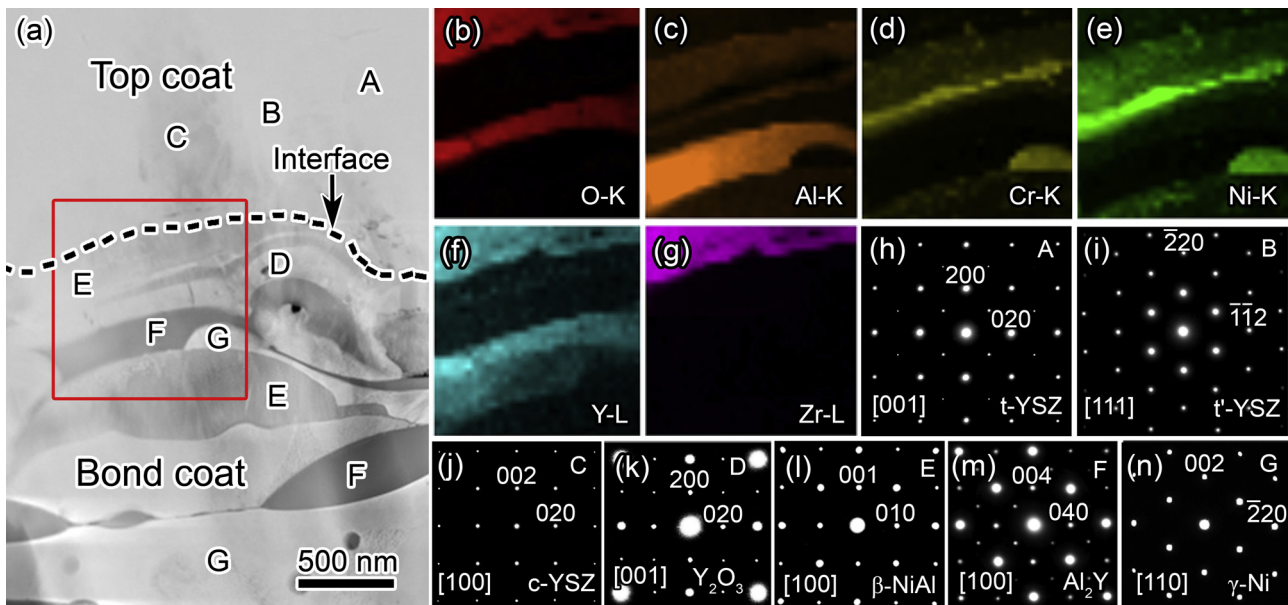
Fig. 4. STEM–EDX element maps of the top coat–bond coat interface in the as-sprayed TBC system and the corresponding selected area electron diffractions (SAEDs). A: tetragonal YSZ (t-YSZ: $P4_2/nmc$, $a = b = 0.361$ nm, $c = 0.518$ nm), B: tetragonal prime YSZ (t′-YSZ: $P4_2/nmc$, $a = b = 0.508$ nm, $c = 0.518$ nm), C: cubic YSZ (c-YSZ: Fm $\bar{3}$ m, $a = 0.513$ nm), D: Y_2O_3 (Ia $\bar{3}$, $a = 1.061$ nm), E: β-NiAl (Pm $\bar{3}$ m, B2 structure, $a = 0.287$ nm), F: Al_2Y (Fd $\bar{3}$ m, $a = 0.786$ nm), G: γ-Ni (Fm $\bar{3}$ m, $a = 0.352$ nm).

a continuous layer at the bond coat–substrate interface (Fig. 10a). Element maps in Fig. 10 show that the TGO layer mainly comprise O (Fig. 10b) and Al (Fig. 10c). Analysis of HRTEM image (Fig. 10g) and its corresponding fast Fourier transformation (FFT) result (Fig. 10h) demonstrates that the phase in the TGO layer is α-Al_2O_3.

Fig. 11 lays out typical element distributions of a representative bond coat-substrate interface after 25 h oxidation. Fig. 11a, a typical HAADF-STEM image of the interface, shows that similar with the TGO at the top coat and bond coat interface after 10 h oxidation (Fig. 7), the TGO layer here also presents two sub-layers as marked with a dashed line. The upper TGO sub-layer is rich in O (Fig. 11b),
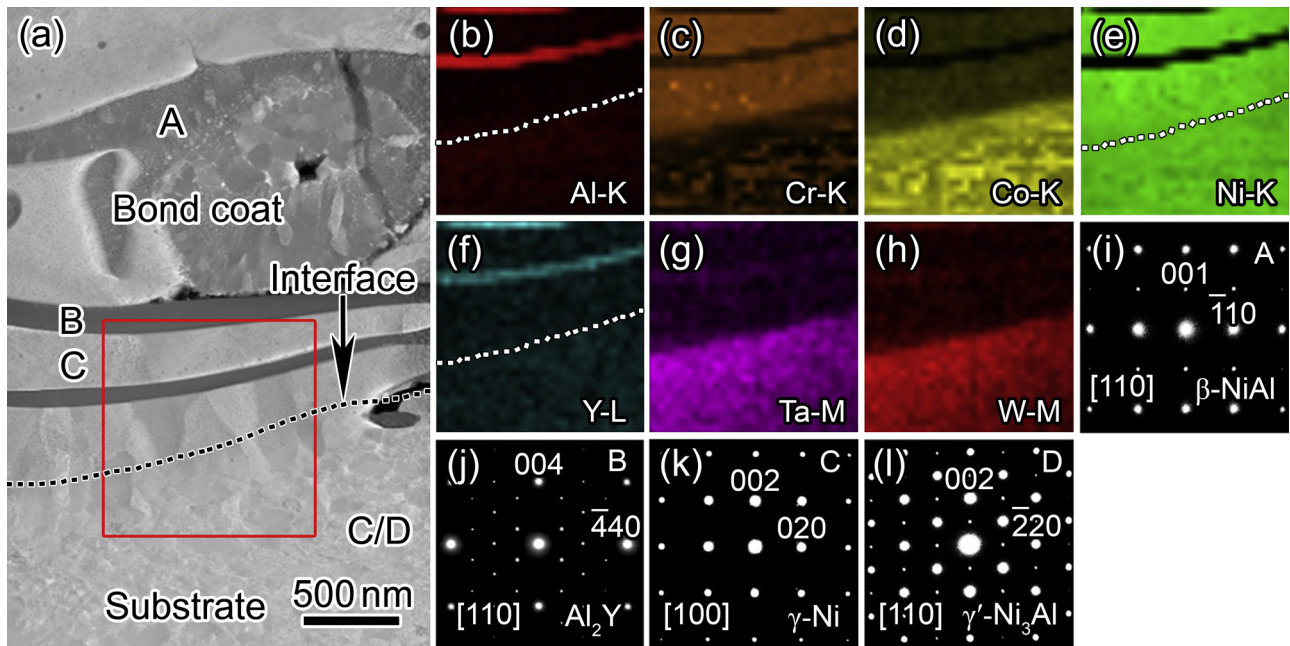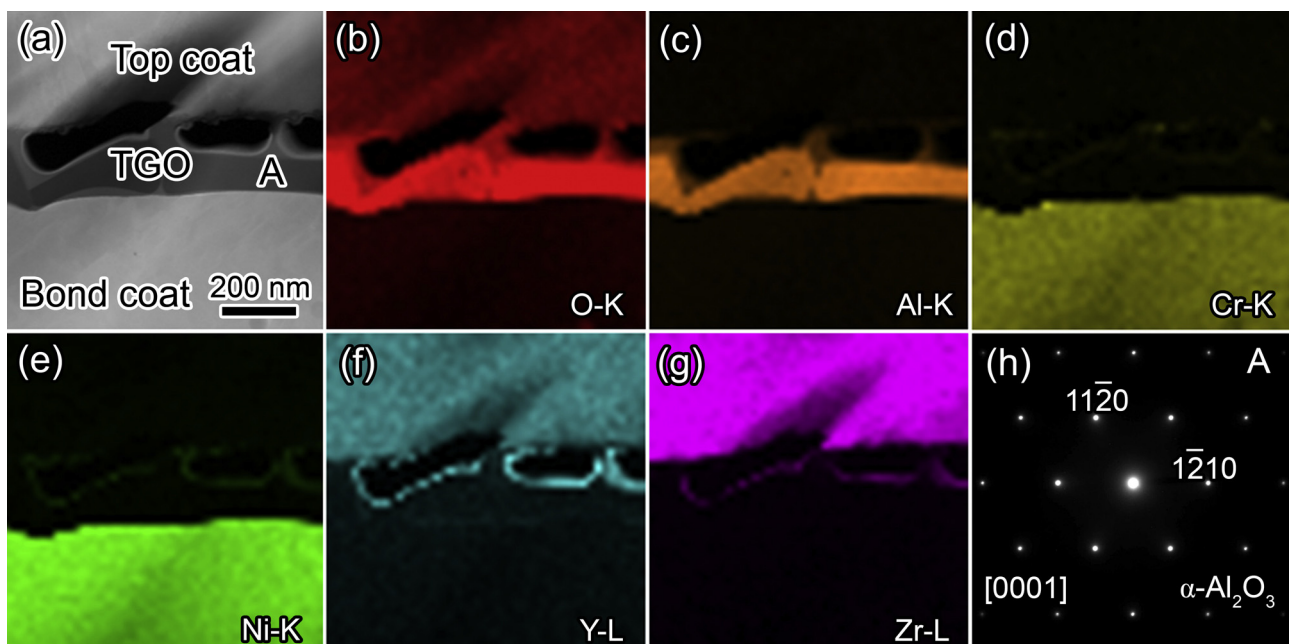
Fig. 5. STEM–EDX element maps of the bond coat-substrate interface in the as-sprayed TBC system and the corresponding SAEDs. D: γ′-Ni₃Al (Pm $\bar{3}$ m, ordered L12 structure, a = 0.357 nm).

Al (Fig. 11c), and Cr (Fig. 11d), which compose α-Al₂O₃, Cr₂O₃, while the lower TGO sub-layer possesses homogeneous α-Al₂O₃. To illustrate Cr₂O₃ in the upper TGO sub-layer, corresponding HRTEM image and its FFT which can be indexed as [10$\bar{1}$0] zone axis have been shown in Fig. 11g and h, respectively.

As depicted in Fig. 12, after 50 h oxidation the TGO layer neighbored to the bond coat is structurally heterogeneous. Except for matrix phase α-Al₂O₃ and Cr₂O₃, the TGO layer also contains other phases such as Ni(Al, Cr)₂O₄ (marked with "A" in Fig. 12a), α-Cr (marked with "B" in Fig. 12a) and γ-Ni (marked with "C" in Fig. 12a). SAED patterns corresponding to Ni(Al, Cr)₂O₄ (Fig. 12g),

α-Cr (Fig. 12h), and γ-Ni (Fig. 12i) were taken from [1 1 1], [1 0 0] and [1 1 1] zone axes, respectively. The TGO layer next to the substrate is homogeneous and has a preponderance of O (Fig. 12b) and Al (Fig. 12c). Interestingly, Al not only segregates in the TGO layer in the form of α-Al₂O₃, but also emerges in the form of pure γ-Al (Fig. 12j) lying in the substrate close to TGO–substrate interface. Furthermore, Ti precipitates both at the TGO–substrate interface and in the substrate as β-Ti (Fig. 12k). The SAED patterns corresponding to γ-Al (Fig. 12j) and β-Ti (Fig. 12k) are acquired from [0 1 0] and [0 0 1] zone axes, respectively.

Fig. 6. STEM–EDX element maps of the top coat–bond coat interface after oxidation at 1100 °C for 5 h and the corresponding SAEDs. A: α-Al₂O₃ (R $\bar{3}$ c, a = 0.476 nm, c = 1.299 nm).
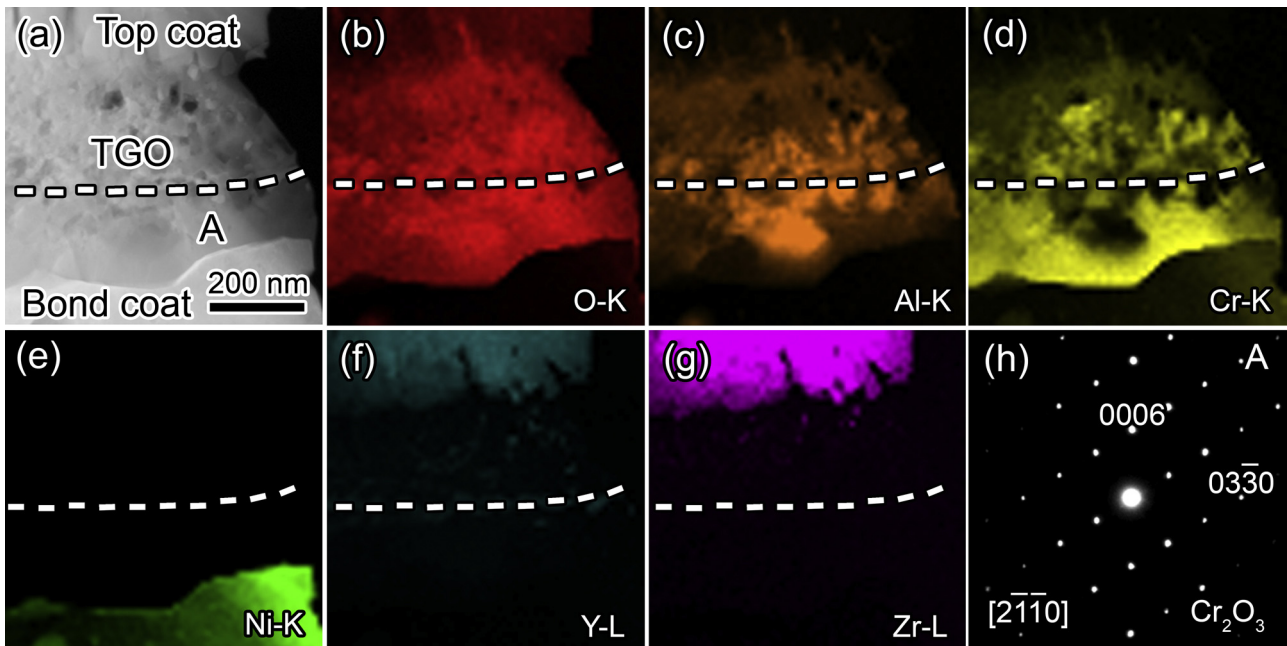
Fig. 7. STEM–EDX element maps of the top coat bond coat interface after oxidation at 1100 °C for 10 h and the corresponding SAED. A: Cr_2O_3 (R $\bar{3}$c, $a = 0.496$ nm, $c = 1.359$ nm).

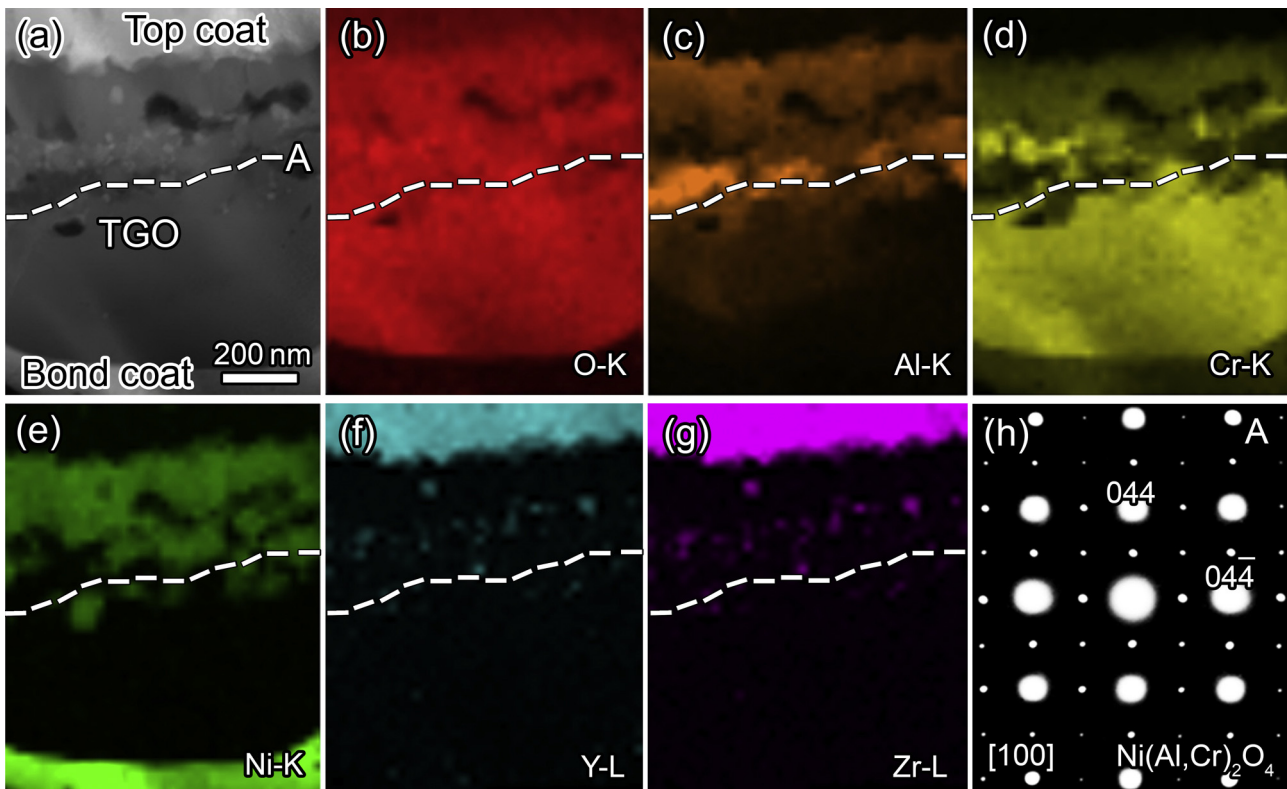**Fig. 8.** STEM–EDX element maps of the top coat–bond coat interface after oxidation at 1100 °C for 25 h and the corresponding SAED. A: Ni(Al, Cr)$_2$O$_4$ (Fd $\bar{3}$ m, a = 0.805 nm).

4. Discussion

### 4.1. A summary of microstructural evolution at interfaces of the TBCs

In order to give a visualized prospect, we summarize the microstructural evolution at both the top coat–bond coat and the bond coat–substrate interfaces as following:

Microstructural evolution at the top coat–bond coat interface

(a) As-sprayed: (top coat) t-YSZ, t′-YSZ, c-YSZ, Y_2O_3 + (bond coat) γ-Ni, β-NiAl and Al$_2$Y.
(b) 5 h: thermally grown α-Al$_2$O$_3$.
(c) 10 h: thermally grown α-Al$_2$O$_3$ and Cr$_2$O$_3$.
(d) 25 h: thermally grown α-Al$_2$O$_3$, Cr$_2$O$_3$ and Ni(Al, Cr)$_2$O$_4$.
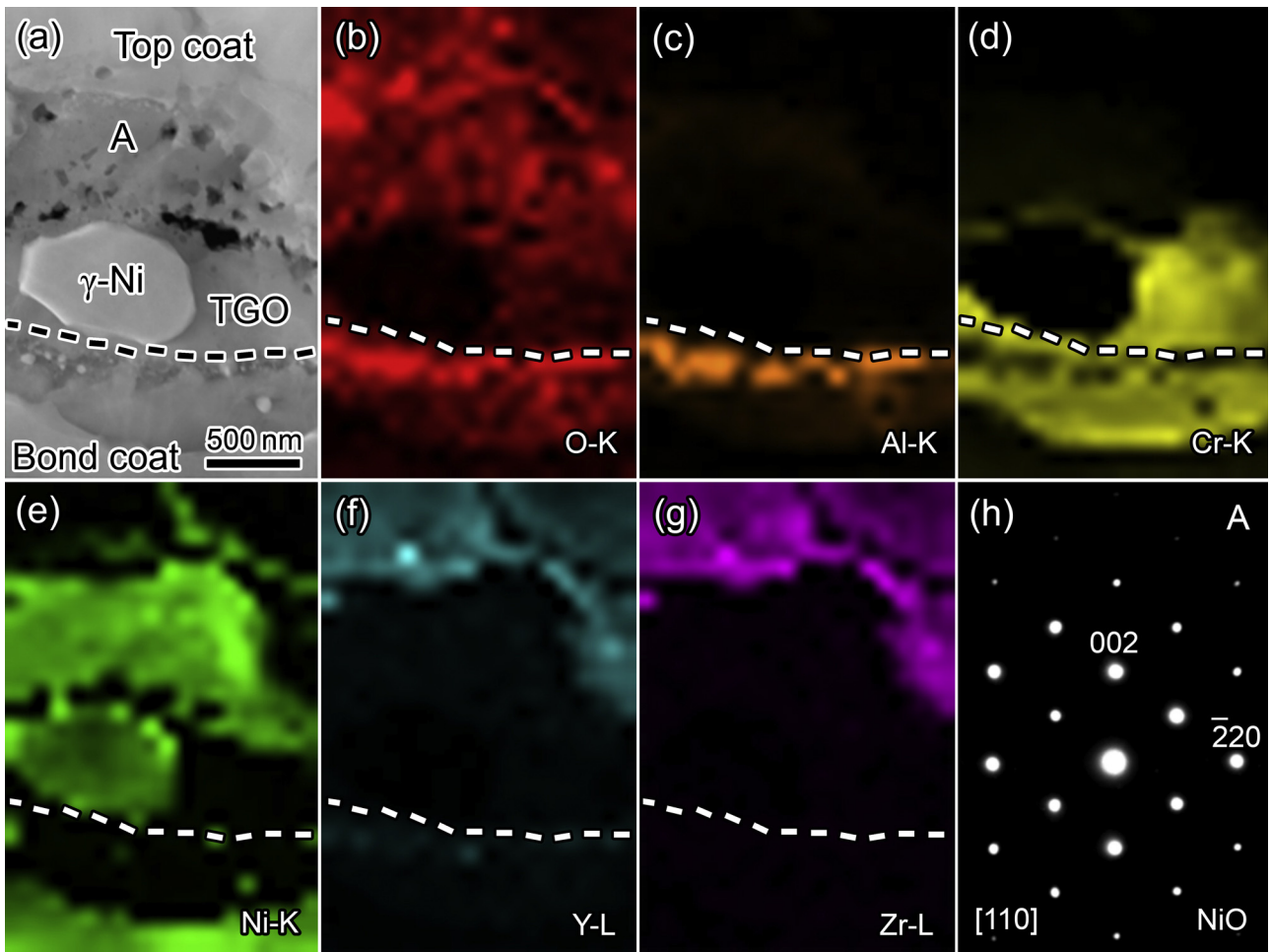
Fig. 9. STEM–EDX element maps of the top coat-bond coat interface after oxidation at 1100 °C for 50 h and the corresponding SAED. A: NiO (Fm $\bar{3}$m, NaCl type structure, a = 0.417 nm).
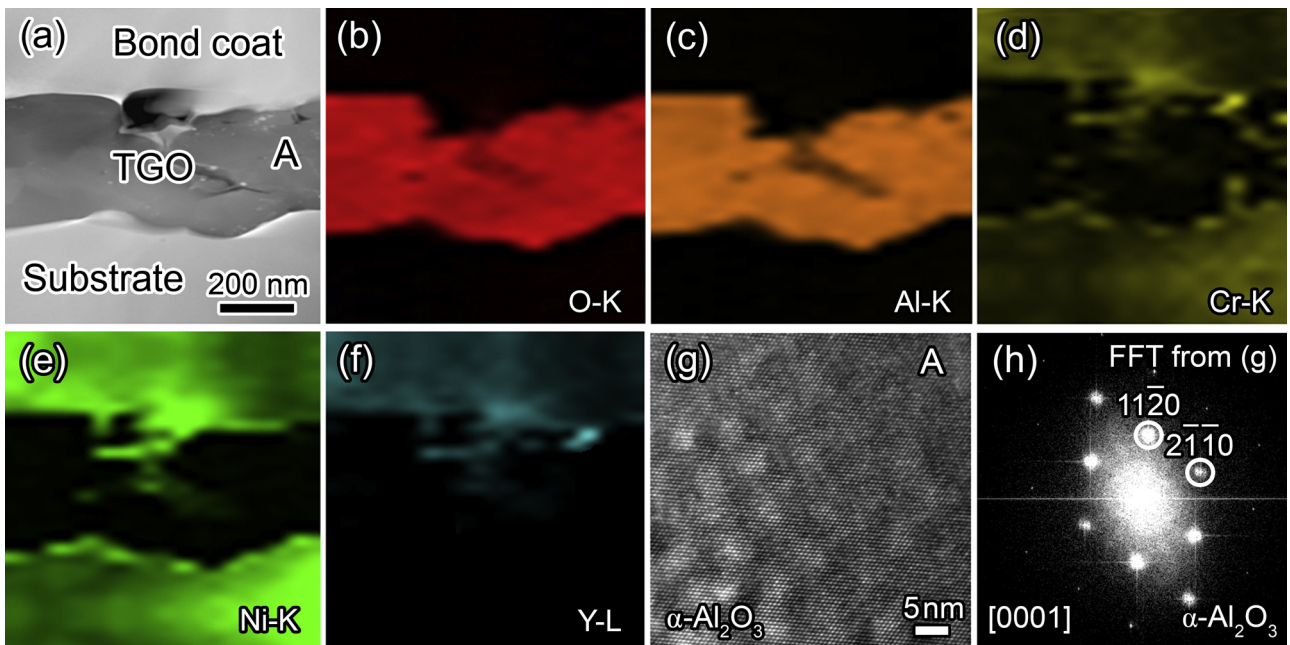
Fig. 10. STEM–EDX element maps of the bond coat-substrate interface after oxidation at 1100 °C for 10 h and the corresponding HRTEM & FFT.
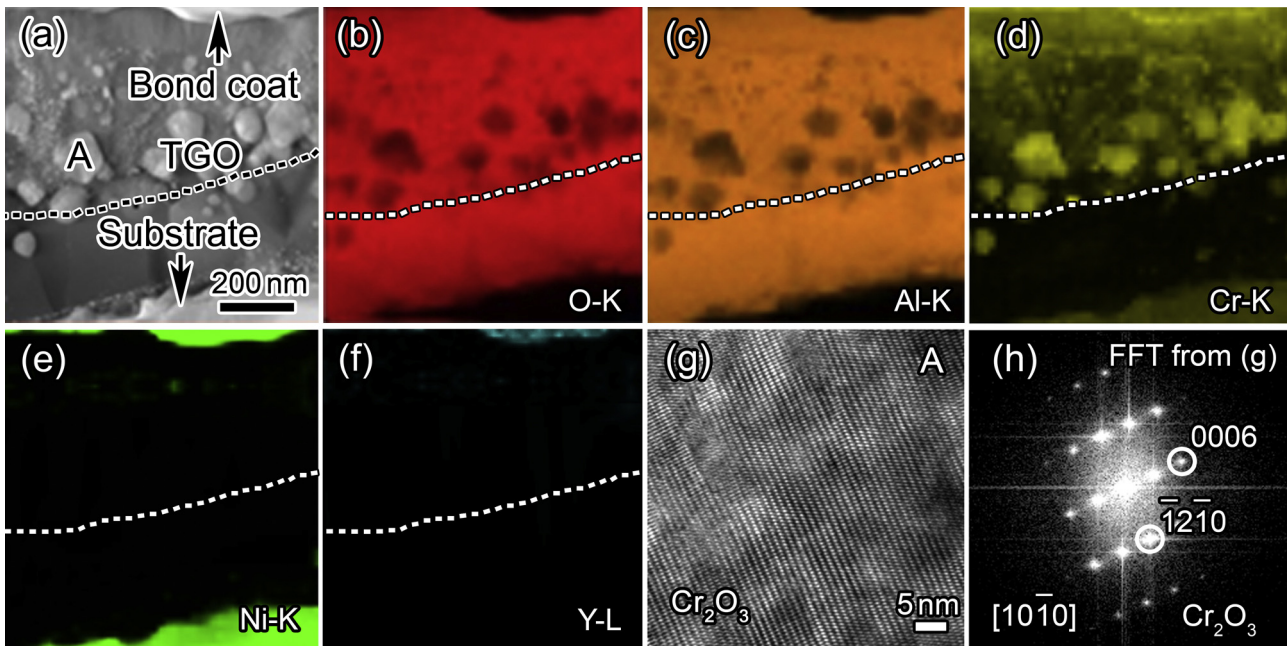
Fig. 11. STEM–EDX element maps of the bond coat-substrate interface after oxidation at 1100 °C for 25 h and the corresponding HRTEM & FFT.
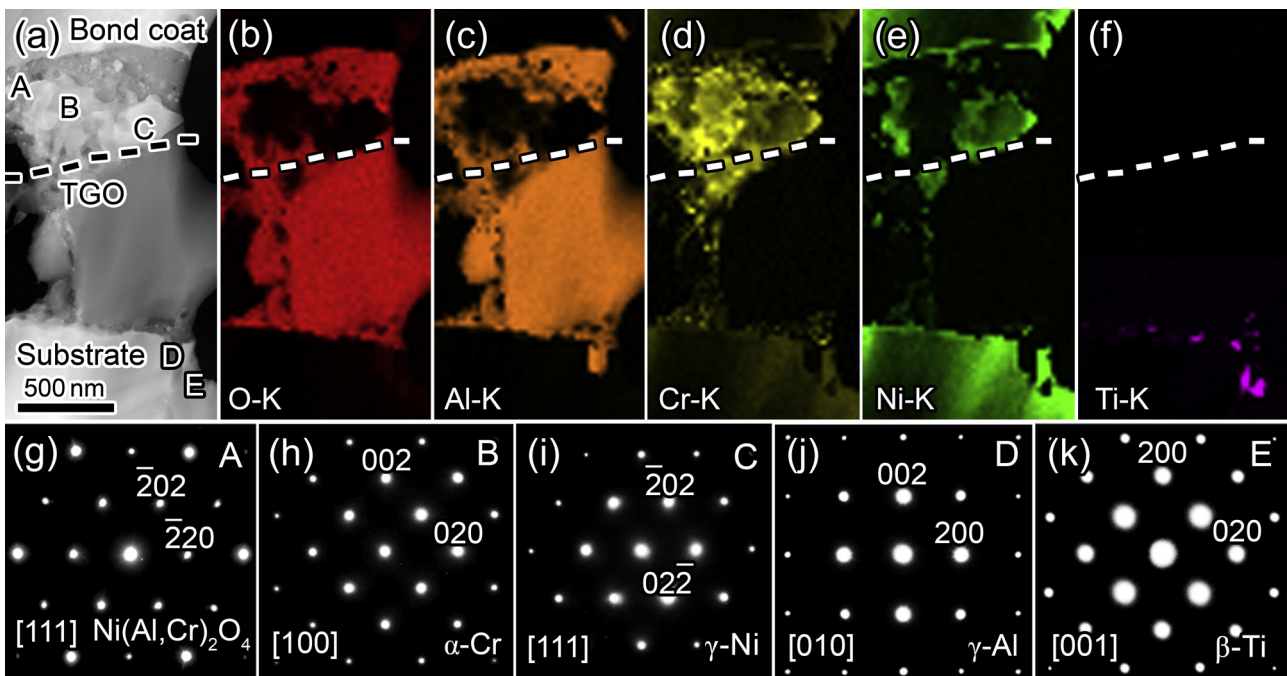

Fig. 12. STEM–EDX element maps of the bond coat–substrate interface after oxidation at 1100 °C for 50 h and the corresponding SAEDs. B: α-Cr (Im $\bar{3}$ m, a = 0.291 nm), D: γ-Al (Fm $\bar{3}$ m, a = 0.403 nm), E: β-Ti (Im $\bar{3}$ m, a = 0.331 nm).

(e) 50 h: thermally grown α-Al$_2$O$_3$, Cr$_2$O$_3$, Ni(Al, Cr)$_2$O$_4$ and NiO + γ-Ni.

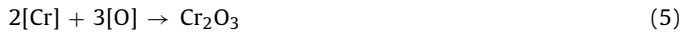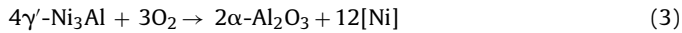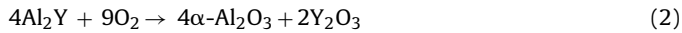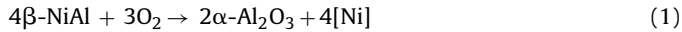Microstructural evolution at the bond coat–substrate interface

(a) As-sprayed: (bond coat) γ-Ni, β-NiAl and Al$_2$Y + (substrate) γ/γ′.
(b) 10 h: thermally grown α-Al$_2$O$_3$.
(c) 25 h: thermally grown α-Al$_2$O$_3$ and Cr$_2$O$_3$.
(d) 50 h: thermally grown α-Al$_2$O$_3$, Cr$_2$O$_3$ and Ni(Al, Cr)$_2$O$_4$ + γ-Ni, α-Cr, γ-Al and β-Ti.

4.1.1. Formation of α-Al$_2$O$_3$- and Cr$_2$O$_3$-rich TGO layers

O is the most important element during the oxidation process. O emerges at the top coa–bond coat and bond coat–substrate interfaces after oxidation at 1100 °C for 5 h (Fig. 6b) and 10 h (Fig. 10b), respectively. Because the as-sprayed top coat has O sublattice, O atom from surface and/or interior of the top coat can easily diffuse across the top coat–bond coat interface and reach the bond coat by means of a discrete hopping process [28], even arrive at the bond coat–substrate interface. With the assistance of interconnected cracks and voids in the as-sprayed ceramic top coat [29], O$_2$ migrates quickly from surface and/or interior of the top coat to the

bond coat. When the O_2 and/or O atom encounter metallic phases (such as β-NiAl, Al_2Y in the bond coat and γ′-Ni_3Al in the substrate) and solute atoms (such as Al and Cr), they will react to form stable oxides owing to high affinities of O with the Al and Cr. As a result, α-Al_2O_3 and Cr_2O_3 form via the following reactions:

$$4β\text{-NiAl} + 3O_2 \rightarrow 2α\text{-}Al_2O_3 + 4[Ni] \qquad (1)$$

$$4Al_2Y + 9O_2 \rightarrow 4α\text{-}Al_2O_3 + 2Y_2O_3 \qquad (2)$$

$$4γ′\text{-}Ni_3Al + 3O_2 \rightarrow 2α\text{-}Al_2O_3 + 12[Ni] \qquad (3)$$

$$2[Al] + 3[O] \rightarrow α\text{-}Al_2O_3 \qquad (4)$$

$$2[Cr] + 3[O] \rightarrow Cr_2O_3 \qquad (5)$$

4.1.2. Formation of Ni(Al, Cr)$_2$O$_4$ in the TGO layers

With depletion of Al and Cr caused by oxidation, Ni starts to react with O and Al_2O_3 to form Ni(Al, Cr)$_2$O$_4$ in the TGO layer between the top coat and the bond coat after 25 h oxidation (Fig. 8h) and in the TGO layer between the bond coat and the substrate after 50 h oxidation (Fig. 12g). A possible Ni(Al, Cr)$_2$O$_4$ formation reaction is given in equation (6).

$$[Ni] + α\text{-}Al_2O_3 + Cr_2O_3 + [O] \rightarrow Ni(Al, Cr)_2O_4 \qquad (6)$$
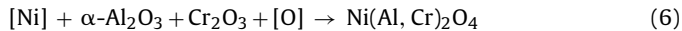
4.1.3. Formation of NiO in the TGO layer between the top coat and the bond coat

Ellingham's diagram [30] indicates that the affinities of metal elements with O increase in an order of Ni, Cr, Al, and the formation energies have the following sequence: $Al_2O_3 < Cr_2O_3 < NiO < 0$. Therefore, NiO only forms at the upper TGO sub-layer at the top coat–bond coat interface until 50 h oxidation (Fig. 9h)which is later than that of α-Al_2O_3 and Cr_2O_3. After the isothermal oxidation at 1100 °C for 50 h, formation of a large number of α-Al_2O_3, Cr_2O_3 and Ni(Al, Cr)$_2$O$_4$ depletes the Al and Cr in the TGO layer. So Ni reacts with the continuous invasive O to produce NiO according to Eq. (7).

$$[Ni] + [O] \rightarrow NiO \qquad (7)$$
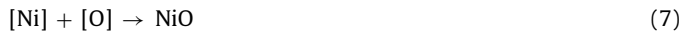
However, at the band coat–substrate interface, even after 50 h oxidation, NiO can not form due to low oxygen partial pressure. NiO is prone to become pulverous at high temperatures ($\geq$1000 °C) [31], so it could degrade TBC systems.

4.1.4. Precipitation of γ-Ni, α-Cr, γ-Al and β-Ti at the TGO-substrate interface

During the oxidation processes, γ-Ni and α-Cr form in the TGO layers, γ-Al and β-Ti precipitate in the substrate next to the TGO–substrate interface. The main reason for the precipitation of pure metal phases is that oxygen partial pressure in the TBC system is low. As for the existence of γ-Ni in the TGO layer between the top coat and the bond coat (Fig. 9a), it should be due to that oxidation consumes solid solution elements Al, Cr, and partial matrix element Ni, extra Ni remains in the form of pure γ-Ni without solid solution element Cr (Figs. 9d and e).

At the bond coat–substrate interface, as the oxidation time prolongs to 50 h, the TGO layers at both the top coat–bond coat interface and the bond coat–substrate interface become thick and they significantly hinders the diffusion of O from the top coat to the bond coat–substrate interface, especially the substrate. At the bond coat–TGO interface, O has reacted with Al completely, but oxygen partial pressure is too low to fully react with superfluous Cr, and Ni. As a result, Ni and Cr precipitate as α-Cr (Fig. 12h) and γ-Ni (Fig. 12i) particles in the upper TGO sub-layer, respectively. Appearance of α-Cr means Cr is excess, so Cr also dissolves in γ-Ni. At the TGO–substrate interface, the Al containing substrate phase γ′-Ni_3Al (Fig. 5l) decomposes into γ-Ni and Al after 50 h oxidation, which is consistent with a previous report [32]. Thus Al can precipitate as

γ-Al. Ti principally solutes in γ′ phase in single crystal superalloys. Because of low solubility in the surrounding phases as well as low oxygen partial pressure, Ti precipitates from the substrate as pure β-Ti phase when the γ′ phases are decomposed. Appearance of γ-Al and β-Ti in the substrate near the TGO–substrate interface may degrade the oxidation resistance of the TBC system. Because γ-Al is prone to be oxidized as α-Al_2O_3 and the β-Ti could transform into fcc-TiN [33] as oxidation time extends. Moreover, the α-Al_2O_3 and fcc-TiN dispersing in the substrate near the TGO layer instead of forming a continuous layer, may destroy the continuity of the TGO layer. However, more experimental evidence is needed to clarify the effects of the γ-Al and β-Ti found here.

4.2. Formation mechanism of TGO sub-layers

The TGO layers at the top coat–bond coat and the bond coat-substrate interfaces split into upper and lower sub-layers when the oxidation time is beyond 10 h and 25 h, respectively. Overall, the upper sub-layer is a mixture of various oxides such as α-Al_2O_3, Cr_2O_3 and Ni(Al, Cr)$_2$O$_4$, while the lower one consists of dense α-Al_2O_3 and/or Cr_2O_3. In the lower TGO sub-layer, the matrix in some areas is α-Al_2O_3 (Fig. 11), but in other areas it is Cr_2O_3 (Fig. 8) after the same oxidation duration. This discrepancy may be caused by overall heterogeneity of the structure and discrete element distribution of Al and Cr in the bond coat.

As discussed above, due to large negative formation energies, α-Al_2O_3 and Cr_2O_3 form first during the oxidation [30], and grow into a continuous α-Al_2O_3 and/or Cr_2O_3 layer. Then, at the side of the α-Al_2O_3 and/or Cr_2O_3 layer close to the surface, Ni (Fig. 6e, Fig. 11e), and top coat containing elements such as Y (Figs. 6–10f), Zr (Figs. 6–8g) accumulate and are embodied by fast grown α-Al_2O_3 and/or Cr_2O_3. The Ni, Y, and Zr embodied in the α-Al_2O_3 and/or Cr_2O_3 layer could form small grains indicated by their dispersive distribution. As a result, the small grains comprising Ni, Y, and Zr prevent α-Al_2O_3 and/or Cr_2O_3 from fast coarsening, and smaller grains appear in the later formed TGO layer. Thus the TGO layer is divided into two sub-layers. Moreover, in the following oxidation, Ni can react with α-Al_2O_3 and Cr_2O_3 to form Ni(Al, Cr)$_2$O$_4$ in both upper sub-layers at the top coat–bond coat interface and the bond–substrate interface. In particular, after 50 h oxidation, formation of NiO in the upper sub-layer at the top coat–bond coat interface, and formation of γ-Ni and α-Cr in the upper TGO sub-layer at the bond coat–substrate interface, enhance the structural difference between the two sub-layers.

5. Conclusion

A typical TBC system with a VPS Ni22Cr10Al1Y bond coat and an APS YSZ (8 wt% Y_2O_3) top coat was fabricated onto a grit-blasting Ni-based single crystal superalloy surface. The as-sprayed samples were isothermally oxidized in air at 1100 °C up to 50 h. The interfacial element segregation and microstructural evolution of the oxidized specimens have been studied by TEM and the following conclusions can be summarized:

(1) TGO layer forms at the top coat–bond coat after 5 h oxidation, and forms at the bond coat-substrate interface after 10 h oxidation. The TGO layers at both the top coat–bond coat and bond coat–substrate interfaces split into upper and lower sub-layers beyond 10 h and 25 h oxidation, respectively. Overall, the upper sub-layer is a mixture of α-Al_2O_3, Cr_2O_3 and Ni(Al, Cr)$_2$O$_4$, while the lower sub-layer mainly consists of dense α-Al_2O_3 and/or Cr_2O_3.

(2) At both the top coat–bond coat and bond coat–substrate interfaces, as oxidation time extends, the phase evolution

follows a procedure: original phases $\rightarrow$ α-Al_2O_3 + Cr_2O_3 $\rightarrow$ α-Al_2O_3 + Cr_2O_3 + $Ni(Al, Cr)_2O_4$. NiO only forms in the upper TGO sub-layer at the top coat–bond coat interface after 50 h oxidation.

(3) Pure metal phases have been identified in the samples after 50 h oxidation. γ-Ni emerges in the upper TGO sub-layers at both top coat–bond coat and bond coat–substrate interfaces after 50 h oxidation. α-Cr can only be seen in the upper TGO sub-layers at the bond coat–substrate interface. γ-Al and β-Ti precipitate in the substrate close to the TGO–substrate interface after 50 h oxidation.

Acknowledgments

References

[1] N.P. Padture, M. Gell, E.H. Jordan, Thermal barrier coatings for gas–turbine engine applications, Science 296 (2002) 280–284.

[2] B.K. Jang, H. Matsubara, Microstructure of nanoporous yttria–stabilized zirconia films fabricated by EB–PVD, J. Eur. Ceram. Soc. 26 (2006) 1585–1590.

[3] S. Guessasma, C. Coddet, Microstructure of APS alumina–titania coatings analysed using artificial neural network, Acta Mater. 52 (2004) 5157–5164.

[4] W.Y. Lee, D.P. Stinton, C.C. Berndt, F. Erdogan, Y.D. Lee, Concept of functionally graded materials for advanced thermal barrier coating applications, J. Am. Ceram. Soc. 79 (1996) 3003–3012.

[5] G.W. Goward, Progress in coatings for gas turbine airfoils, Surf. Coat. Technol. 108 (1998) 73–79.

[6] S.M. Meier, D.K. Gupta, The evolution of thermal barrier coatings in gas turbine engine applications, Trans. ASME 116 (1994) 250–257.

[7] A.K. Ray, R.W. Steinbrech, Crack propagation studies of thermal barrier coatings under bending, J. Eur. Ceram. Soc. 19 (1999) 2097–3009.

[8] M.P. Taylor, H.E. Evans, E.P. Busso, Z.Q. Qian, Creep properties of a Pt–aluminide coating, Acta Mater. 54 (2006) 3241–3252.

[9] M.S. Ali, S.H. Song, P. Xiao, Evaluation of degradation of thermal barrier coatings using impedance spectroscopy, J. Eur. Ceram. Soc. 22 (2002) 101–107.

[10] A. Rabiei, A.G. Evans, Failure mechanisms associated with the thermally grown oxide in plasma–sprayed thermal barrier coatings, Acta Mater. 48 (2000) 3963–3976.

[11] D. Liu, M. Seraffon, P.E.J. Flewitt, N.J. Simms, J.R. Nicholls, D.S. Richerby, Effect of substrate curvature on residual stresses and failure modes of an air plasma sprayedthermal barrier coating system, J. Eur. Ceram. Soc 33 (2013) 3345–3357.

[12] H.C. Chen, J. Heberlein, E. Pfender, TEM characterization of plasma–sprayed thermal barrier coatings and ceramic–metal interfaces after hot isostatic pressing, Thin Solid Films 301 (1997) 105––114.

[13] S.Q. Guo, Y. Tanaka, Y. Kagawa, Effect of interface roughness and coating thickness on interfacial shear mechanical properties of EB-PVD yttria–partially stabilized zirconia thermal barrier coating systems, J. Eur. Ceram. Soc. 27 (2007) 3425–3431.

[14] S.S. Kim, Y.F. Liu, Y. Kagawa, Evaluation of interfacial mechanical properties under shear loading in EB-PVD TBCs by the pushout method, Acta Mater. 55 (2007) 3771–3781.

[15] H.X. Chen, K.S. Zhou, Z.P. Jin, C.L. Liu, Diffusion and phase transformation on interface between substrate and bond coat in Y-PSZ thermal barrier coatings, J. Therm. Spray Technol. 13 (2004) 515–520.

[16] R.T. Wu, R.C. Reed, On the compatibility of single crystal superalloys with a thermal barrier coating system, Acta Mater. 56 (2008) 313–323.

[17] J.E. Schilbe, Substrate alloy element diffusion in thermal barrier coatings, Surf. Coat. Technol. 133–134 (2000) 35––39.

[18] S. Ahmaniemi, M. Vippola, P. Vuoristo, T. Mäntylä, F. Cernuschi, L. Lutterotti, Modified thick thermal barrier coatings: microstructural characterization, J. Eur. Ceram. Soc. 24 (2004) 2247–2258.

[19] R. Molins, I. Rouzou, P.Y.A. Hou, TEM study of sulfur distribution in oxidized Ni40Al and its effect on oxide growth and adherence, Mater. Sci. Eng. A 454–455 (2007) 80–88.

[20] P. Poza, J. Gómez-García, C.J. Múnez, TEM analysis of the microstructure of thermal barrier coatings after isothermal oxidation, Acta Mater. 60 (2012) 7197–7206.

[21] B.W. Kempshall, Y.H. Sohn, S.K. Jha, S. Laxman, R.R. Vanfleet, J. Kimmel, A microstructural observation of near–failure thermal barrier coating: a study by photostimulated luminescence spectroscopy and transmission electron microscopy, Thin Solid Films 466 (2004) 128–136.

[22] M.J. Stiger, N.M. Yanar, M.G. Topping, F.S. Pettit, G.H. Meier, Thermal barrier coatings for the 21st century, Z Metallkd. 90 (1999) 1069–1078.

[23] R. Vassen, X.Q. Cao, F. Tietz, D. Basu, D. Stöver, Zirconates as new materials for thermal barrier coatings, J. Am. Ceram. Soc. 83 (2000) 2023–2028.

[24] U. Schulz, M. Menzebach, C. Leyens, Y.Q. Yang, Influence of substrate material on oxidation behavior and cyclic lifetime of EB-PVD TBC systems, Surf. Coat. Technol. 146 (2001) 117–123.

[25] U. Schulz, C. Leyens, K. Fritscher, P. Manfred, S.B. Bilge, L. Odile, J.M. Dorvaux, M. Poulain, R. Mévrel, M. Caliez, Some recent trends in research and technology of advanced thermal barrier coatings, Aerosp. Sci. Technol. 7 (2003) 73–80.

[26] Z. Chen, S. Speakman, J. Howe, H. Wang, W. Porter, R. Trice, Investigation of reactions between vanadium oxide and plasma–sprayed yttria–stabilized zirconia coatings, J. Eur. Ceram. Soc. 29 (2009) 1403–1411.

[27] D.R. Clarke, S.R. Phillpot, Thermal barrier coating materials, Mater. Today 8 (2005) 22–29.

[28] H.W. Brinkman, W.J. Briels, H. Verweij, Molecular dynamics simulations of yttria–stabilized zirconia, Chem. Phys. Lett. 247 (1995) 386––390.

[29] A.C. Fox, T.W. Clyne, Oxygen transport by gas permeation through the zirconia layer in plasma sprayed thermal barrier coatings, Surf. Coat. Technol. 184 (2004) 311–321.

[30] H. Ellingham, Reducibility of oxides and sulfides in metallurgical processes, J. Soc. Chem. Ind. 63 (1944) 125–133.

[31] M. Göbel, A. Rahmel, M. Schütze, The isothermal–oxidation behavior of several nickel-base single-crystal superalloys with and without coatings, Oxid. Met. 39 (1993) 231–261.

[32] W.Z. Li, Y.Q. Li, C. Sun, Z.L. Hu, T.Q. Liang, W.Q. Lai, Microstructural characteristics and degradation mechanism of the NiCrAlY/CrN/DSM11 system during thermal exposure at 1100 °C, J. Alloy Compd. 506 (2010) 77–84.

[33] Y.Z. Liu, X.B. Hu, S.J. Zheng, Y.L. Zhu, H. Wei, X.L. Ma, Microstructural evolution of the interface between NiCrAlY coating and superalloy during isothermal oxidation, Mater. Design 80 (2015) 63–69.